EPJ D
Atomic, Molecular, Optical and Plasma Physics
EPJ.org
your physics journal

Eur. Phys. J. D (2013) 67: 268 DOI: 10.1140/epjd/e2013-40434-5

Electron angular distributions and attachment rates in o-Benzyne and Phenyl aromatic molecules: the effect of the permanent dipoles

Fabio Carelli and Franco A. Gianturco

edp sciences
Società Italiana di Fisica
Springer

Eur. Phys. J. D (2013) 67: 268
DOI: 10.1140/epjd/e2013-40434-5

THE EUROPEAN PHYSICAL JOURNAL D

Regular Article

Electron angular distributions and attachment rates in o-Benzyne and Phenyl aromatic molecules: the effect of the permanent dipoles*

Fabio Carelli and Franco A. Gianturco[a]

Department of Chemistry and CISM, The University of Rome 'Sapienza', P.le Aldo Moro 5, 00185 Rome, Italy

Received 22 July 2013 / Received in final form 31 August 2013
Published online 17 December 2013 –

Abstract. Free, gas-phase polycyclic aromatic hydrocarbons (PAHs) and related species are currently considered to play an important role in the interstellar/circumstellar medium as they are thought to significantly contribute to both Diffuse and Unidentified infrared interstellar bands. They are also considered fundamental blocks of the interstellar dust and several formation mechanisms were proposed with regard to their interstellar/circumstellar synthesis. In this paper we therefore present and discuss the results obtained from ab initio quantum scattering calculations of the response from neutral polar aromatic single-ring species to low-energies electron collisions. Our main purpose is here to provide new values for the rate constants for electron attachment to orthobenzyne and to phenyl molecules by discussing in detail the effects of the long-range dipole interaction in the framework of the Born perturbative approximation at the first order. We shall further discuss the specific behavior of the electrons' diffusion by such molecules, especially in the low-energy range of the scattered particles' energies as guided by their permanent dipole moments. We shall also provide accurate numerical fittings for both rates and give explicitly the fitting parameters for their possible use in evolutionary models.

1 Introduction

Polycyclic aromatic hydrocarbons (PAHs) are large molecules with carbon atoms arranged in five- or six-membered rings. They are known to be abundant and ubiquitous in the interstellar medium (ISM) [1–5], even though currently no specific chemical carrier has been identified [6,7] with the exception of benzene (C_6H_6) [8]. These molecules are also taken as prebiotic species (as important carbon-bearing species) [9] and are surmised to lock up ∼5% of the elemental carbon, hence representing a carbon reservoir which is comparable to that of gaseous CO [10].

In connection with the molecular synthesis which are taken to occur in the stellar wind of C-rich AGB stars, at present it is well known that the carbon element, synthesized through helium burning reactions in the core of the star, is then dredged up to the photosphere due to convective transport mechanisms so that it reacts there with the elemental oxygen forming CO, while the excess carbon can additionally form other carbon-based molecules (like C_2) that constitute the starting point for the synthesis of the acetylene, C_2H_2, (mainly due to the wide availability of hydrogen in the outer shell), the most diffuse carbon-bearing species in the ISM and, from the astrochemical point of view, the fundamental building block for the possible subsequent formation of aromatic rings.

Since AGB stars undergo extensive mass loss at typically high rates, (up to 10^{-4} $M\,yr^{-1}$) [11,12], the circumstellar material is physically processed through an intense stellar wind; accordingly, free gas-phase PAHs are thought to form either in the ejecta from C-rich post-AGB stars or in evolved proto-planetary nebulae (PPN) objects as critical intermediaries and by-products of the dust formation processes. In line with that, in fact, both cristalline and amorphous solid-state nanoparticles are surmised to be condensed in the above stellar wind to such an extent that the circumstellar envelope, in the late stage of the AGB phase evolution, can nearly completely obscure the central star by dust extinction [13], where such a thick molecular envelope might survive during the beginning of the next planetary nebula (PN) phase [14] as observations suggest [15,16]. It therefore follows that the spectroscopic detection of organic aromatic compounds, both in the circumstellar environments (CSE) and in the ejecta of C-rich evolved stars, indirectly provide precious information on how these species are formed: hence, the fact that no aromatic infrared bands (AIBs) have been seen in AGB stars, the AIBs making instead their appearence either in the post-AGB or PPN objects, strongly suggests that the

* Contribution to the Topical Issue "Astrochemical Processes and Evolutionary Modelling for Stars and Planetary Systems", edited by Serena Viti, Franco A. Gianturco and Nigel Mason.

[a] e-mail: francesco.gianturco@uniroma1.it

aromatic species might be synthesized mainly during the post-AGB phase of C-rich stars [17–19].

2 Routes to PAHs formation: an outline

Generally speaking, the most favourable routes regarding the interstellar/circumstellar PAHs synthesis were surmised to involve molecular weight growth processes that occurr mainly in warm and dense CSE around evolved C-rich stars through chemical reactions of simple one-ring aromatic species (like the phenyl radical, C_6H_5) with acetylenic radicals (like the propargyl species, HC≡C-CH_2) [20–22] based on the hydrogen-abstraction-acetylene-addition mechanism that operates at high temperatures ($T \sim 1000$ K) [23]. In this connection, some theoretical studies suggest that, at the above temperatures, the naphthalene molecule could be efficiently synthesized by gas-phase mechanisms involving phenyl-radical reactions with the vinyl-acetylene (HC≡C-CH=CH_2) [24], as well as through the reaction of benzene (C_6H_6) with o-benzyne (o-C_6H_4) [25]. Last but not least, also the low-temperature ($T \sim 10$ K) formation of naphthalene in the cold interstellar medium was recently experimentally probed [26]: the authors of that work showed that the naphthalene molecule can be efficiently formed in the gas-phase via a barrierless and exoergic reaction between the phenyl-radical and the vinyl-acetylene species involving the formation of a van-der-Waals transient complex followed by an isomerization of the vinylacetylene via a 'submerged' barrier at much lower temperatures ($T \sim 10$ K) than previously surmised.

Regarding this low-temperature chemical path, as the authors of [27] also mention, it is very important to include the effects of photolysis and interstellar shock waves driven by supernova explosions, as well as those related to the cosmic ray processing. Thus it becomes possible to argue that PAHs in the ISM are destroyed on a relatively short time scale [26,28,29], one which could be shorter than the typical time scale for the injection of new aromatic carbon-rich material into the ISM itself [30]: in order to account for the almost ubiquitous presence of PAHs in the ISM a new and as yet unexplained route is therefore needed to justify the fast chemical growth of PAHs, since a chemical path involving the phenyl species could be active in cold environments like dense and dark molecular clouds. In this sense, even if the C_6H_5 does not properly represent a polycyclic aromatic species, it clearly represents at least one of the building blocks for PAHs formation so that its chemistry and more in general that of benzene-related species (like the aromatic single-ring orthobenzyne, o-C_6H_4, and the phenyl radical C_6H_5) are prototypical toward the formation of larger aromatic species in the above astrophysical environments. In line with such considerations, we additionally think that low-energy collisions with free electrons, whose presence may be found either in the stellar wind or in the local photoionization of interstellar/circumstellar matter (including dense molecular clouds), can participate to the above complex synthetic mechanisms by forming either low-energy 'compound' resonances or virtual states by which it is in turn possible to access a variety of stable negative ions via several energy-redistribution paths.

We have further established in our earlier work [31,32] that another PAH precursor, the closed-shell neutral orthobenzyne, exhibits the presence of marked metastable anionic resonances when interacting with low-energy electrons. Those findings enabled us to suggest direct involvement of its associated anion within the complex chain of reactions leading to the formation of the larger PAHs. It is thus reasonable to now argue that both such single-ring aromatic systems should be involved both in the ISM and in protoplanetary atmospheres. Their electron affinities are known: $EA_{phenyl} = 1.0960 \pm 0.0060$ eV [33], while $EA_{o\text{-}benzyne} = 0.5640 \pm 0.0070$ eV [34] and so are their dipole moments: $\mu_{phenyl} = 0.872$ D/0.9 D, the first computed at the ROB3LYP/aug-cc-pVTZ expansion level by us and the second value experimentally determined by [35], while for the o-C_6H_4 case, $\mu_{o\text{-}benzyne} =$ 1.68 D/1.77 D, the first number referring to one theoretical value [36] and the second also computationally evaluated by us [32] at the B3LYP/aug-cc-pVTZ level.

Although the definitive identification of PAHs species in the ISM has been proven difficult and challenging, they have been tentatively included in some astrochemical models [37–39], where generally speaking their inclusion is shown to have remarkable consequences. In this framework, keeping in mind that the dehydrogenated PAH anions might be more stable in both interstellar and circumstellar environments because of their larger electron affinity (EA) once they become radical PAHs [40], the phenyde ion ($C_6H_5^-$) constitutes a very likely archetype species since the neutral (not deprotonated) counterpart is the benzene molecule which has instead a large positive EA. Since the astrochemical models that currently include PAHs do not yet account for the dehydrogenated anionic polycyclic aromatic species (generally identified as PAH^-_{n-1}), it is important to start to characterize the kinetics of formation of this class of anions: accordingly, we have already discussed earlier [41] the mechanisms that, at the nanoscopic level, can yield the phenyde metastable anion as the doorway for the formation of the thermodynamically stable phenyde anion, whose gas-phase reactivity with species of interstellar relevance has been recently experimentally probed [42] with very similar conclusions.

The main purpose of our present work is instead to further analyse in some detail the role of the permanent dipole moments of the two title molecules on the accurate determination of their behavior when scattering electrons at very low-energies, i.e. the quantum deflections of free electrons which may be caused by both molecules in the gas phase.

Hence, to reliably obtain differential cross sections (DCS) for the scattered electrons shall provide useful indicators on the efficiency of the title molecules to electron deflection. It shall also give us essential information, at very low temperatures, on the corresponding electron attachment rates that can be employed in evolutionary models that include these anions among the network of

chemical processes relevant to ISM environments. In this respect, therefore, to go from DCS to integral cross sections (ICS) and then to electron attachment rates for polar molecules will be one of the tasks of the present study.

3 The computational model

3.1 electron-molecule scattering: elastic cross sections

Since the quantum dynamical equations used for this study have been described in detail many times before [43,44], we only present here a brief outline of them and refer the interested reader to those earlier publications.

The total $(N+1)$-electron wavefunction is constructed as an antisymmmetrized product of one-electron wave functions obtained from Hartree-Fock orbitals of the neutral ground state molecular target, considering the N bound electrons in their ground-state configuration during the whole scattering process: thus, no core-excited resonances are allowed in our modelling. The nuclear configuration of the molecular target is fixed at its equilibrium structure during the whole collisional event, which gives back the fixed nuclei (FN) approximation. Each of the three dimensional wave functions describing a given electron is expanded around the molecular center of mass (Single Center Expansion, SCE, [43]) so that for each of the bound molecular electrons we have

$$\phi_i^{p\mu} = \frac{1}{r}\sum_{\ell h} u_{\ell h}^{p\mu,i}(r)\chi_{\ell h}^{p\mu}(\hat{r};\mathbf{R}) \tag{1}$$

and for the scattered particle

$$\psi^{p\mu} = \frac{1}{r}\sum_{\ell h} f_{\ell h}^{p\mu}(r)\chi_{\ell h}^{p\mu}(\hat{r};\mathbf{R}). \tag{2}$$

In the above SCE representations, the superscripts label the μth irreducible representation of the pth symmetry group to which the molecule belongs at the fixed nuclear geometry $\mathbf{R}$, and the subscripts refer to each of the angular channels under consideration; the radial coefficients $u_{\ell h}^{p\mu,\alpha}$ for the bound molecular electrons are numerically evaluated by a quadrature on a radial grid [45]. The angular functions $\chi_{\ell h}^{p\mu}$ are symmetry adapted angular functions given by proper combinations of the spherical harmonics

$$\chi_{\ell h}^{p\mu} = \sum_m b_{\ell h m}^{p\mu} Y_\ell^m(\hat{r}), \tag{3}$$

where the $b_{\ell h m}^{p\mu}$ coefficients are described and tabulated in reference [46].

The ensuing coupled partial integro-differential equations provide us with a way of evaluating the unknown radial coefficients $f_{\ell h}^{p\mu}$ for the $(N+1)$th continuum electron, scattered off the N-electron neutral target, by using the SCE radial quantities for the occupied molecular orbitals [47]

$$\left[\frac{d^2}{dr^2} - \frac{l(l+1)}{r^2} + 2\,(E-\epsilon)\right] f_{lh}^{p\mu}(r|\mathbf{R}) = 2\sum_{l'h'}\int dr' \hat{V}_{lh,l'h'}^{p\mu}(r,r'|\mathbf{R}) f_{l'h'}^{p\mu}(r'|\mathbf{R}), \tag{4}$$

where E is the collision energy $E = k^2/2$ and ϵ is the eigenvalue for the electronic ground state energy so that $(k^2/2 = E-\epsilon)$, k being the asymptotic momentum of the elastically scattered electron.

As previously anticipated, the assumption that the target molecule is here realistically described by its electronic ground-state obtains the static-exchange (SE) representation of the electron-molecule interaction for the molecular ground-state geometry $\mathbf{R}$. For a target which has a closed shell electronic structure, with $n_{occ} = N/2$ doubly occupied molecular orbitals, the SE potential has the following form:

$$V_{SE}(\mathbf{r}) = \sum_{\gamma=1}^{M}\frac{Z_\gamma}{|\mathbf{r}-\mathbf{R}_\gamma|} + \sum_{i=1}^{n_{occ}}\left(2\hat{J}_i - \hat{K}_i\right) = V_{st} - \sum_{i=1}^{n_{occ}}\hat{K}_i \tag{5}$$

where $\hat{J}_i$ and $\hat{K}_i$ are the usual local static potential and the non-local exchange potential operators respectively. The index γ runs over the M molecular nuclei within the center of mass frame. The SE approach, however, does not include the dynamical response of the target to the impinging electron, i.e. the correlation and polarization effects acting at short and at large electron-target distances respectively. Thus, we model the above additional part of the overall interaction by introducing the following optical potential:

$$V_{cp}(r) = \begin{cases} V_{corr}(r) & \text{for } r \le r_{match} \\ V_{pol}(r) & \text{for } r > r_{match}. \end{cases} \tag{6}$$

We further employ the Free-Electron-gas-exchange model proposed by Hara (HFEGE), [48], V_{HFEGE}

$$V_{HFEGE}(\mathbf{r}|\mathbf{R}) = -\frac{2}{\pi}K_F(\mathbf{r}|\mathbf{R})\left[\frac{1}{2} + \frac{1-\eta^2}{4\eta}\ln\left(\frac{1+\eta}{1-\eta}\right)\right], \tag{7}$$

where the wavevector up to the top of the Fermi surface is given by the usual free-electron relation

$$K_F(\mathbf{r}|\mathbf{R}) = \left[3\pi^2\rho(\mathbf{r}|\mathbf{R})\right]^{1/3}, \tag{8}$$

and $\eta(\mathbf{r})$ holds the ratio between the actual wavevector $k(\mathbf{r})$ for the scattered electronic particle and the one at the top of the Fermi surface for the free-electron gas.

For the present case, since we are dealing also with an *open*-shell system (the phenyl radical), the electronic density $\rho(\mathbf{r}|\mathbf{R})$

$$\rho(\mathbf{r}) = \int |det||\phi_1(\mathbf{r})\phi_2(\mathbf{x}_2)\cdots\phi_{n_e}(\mathbf{x}_{n_e})|||^2 d\mathbf{x}_2\cdots d\mathbf{x}_{n_e} \tag{9}$$

is evaluated by assigning 2 as the occupation number of each of the 20 doubly occupied MO in the neutral target (as we do for the o-benzyne) and by setting instead such value to 1 for the X^2A_1 single electron in the phenyl radical: in this way we treat 'exactly' (in the limit of the HFEGE local energy-dependent scheme) the exchange interaction between the colliding electron and each of the 'core' doubly occupied MOs, while keeping for the uncoupled bound electron an 'hybrid' description which is in between a triplet/singlet.

This last step provides the so-called static-model-exchange-correlation-polarization (SMECP) approximation for the scattering event. The coupled set of integrodifferential equations in equation (4) now takes the form

$$\left[\frac{d^2}{dr^2} - \frac{l(l+1)}{r^2} + k^2\right] f_{lh}^{p\mu}(r) = 2\sum_{l'h'} V_{lh,l'h'}^{p\mu}(r) f_{l'h'}^{p\mu}(r), \tag{10}$$

where the potential coupling elements are now given by

$$\begin{aligned} V_{lh,l'h'}^{p\mu}(r) &= \langle \chi_{lh}^{p\mu}(\hat{r})|V(\mathbf{r})|\chi_{l'h'}^{p\mu}(\hat{r})\rangle \\ &= \int d\hat{r}\chi_{lh}^{p\mu}(\hat{r})V(\mathbf{r})\chi_{l'h'}^{p\mu}(\hat{r}). \end{aligned} \tag{11}$$

We numerically solve the coupled equations equation (10) using $V = V_{SMECP}$ to produce both the K-matrix elements and the scattering amplitude in the body-fixed (BF) frame of reference, the latter being centered on the molecular center of mass with the 'z' axis along the highest symmetry axis at the given nuclear geometry.

To provide physically meaningful quantities which could be compared with experiments, when available, we have however to express the BF scattering amplitude in the laboratory frame (space-fixed, SF), in which the axis are arbitrarily oriented and kept fixed during the collision, so that the squared modulus of the latter quantity enables us to express the differential cross section (DCS) as

$$\begin{aligned} \frac{d\sigma}{d\Omega} &= \frac{1}{8\pi^2}\int d\alpha\ \sin\beta\, d\beta\, d\gamma\, |f(\hat{k}\hat{r}|\alpha,\beta,\gamma)|^2 \\ &= \sum_L A_L P_L(\cos\theta) \end{aligned} \tag{12}$$

where α, β and γ refer to the Euler angles, so that in the last formula θ is now the center of mass angle from the impinging direction $\hat{k}$ (in the BF frame of reference); while the A_L coefficients are found to be directly dependent on the $K_{\ell,\ell'}$ elements as rather complicated functions of the colliding electron orbital angular momentum ℓ [49]. It should be mentioned at this point that all the above computed observables were obtained through the use of our own developed computational codes.

3.2 Dipole interaction and angular distributions: the Born correction and the rotationally inelastic cross sections

For polar targets, the calculation of the K-matrix in any frame of reference when using the FN approximation yields a logaritmic divergence of the ICS, which in turn comes from the divergence in the forward direction that characterizes the total DCS, [44].

The above breakdown basically depends on the long-range nature of the interaction potential that, for the dipole term, turns out to be the strongest at large distances ($V_\mu \sim 1/r^2$, r being the distance between the incoming electron and the molecular center of mass). The collision cross section, in qualitative terms, can be thought of as being due to two distinct parts: the first includes the contributions of the smaller partial waves to the K-matrix elements, while the second accounts for the contributions from the larger ℓ, ℓ' values associated to a colliding electron sampling very large centrifugal barriers that in principle should keep it away from the inner region. It follows that the phase shifts of the latter contributions will be mainly caused by the long range part of the potential so that, in this region, the impinging electron experiences a pure dipole potential normally weak enough that the first order perturbation of the Born approximation (FBA) can be safely used to describe its effects. The angular distribution of the scattered electron by a point dipole of fixed orientation (i.e. *non* rotating) has a simple pole for $\theta = 0$ when the collisional problem is solved in the FBA [50]. Moreover, it can additionally be shown that if one tries to evaluate the DCS via a series expansion (like in Eq. (12)), oscillating contributions will begin to arise when the size of the involved partial waves is increased [51].

In order to remedy this, while still taking advantage of the intrinsic simplicity of the FN approximation in the framework of the adiabatic nuclei rotational (ANR) scheme, we used the well-known multipole-extracted-adiabatic-nuclei approximation (MEAN) [51]. This approach enables us to avoid the divergence problem by using a closure formula that also accounts for molecular rotational transitions $J' \leftarrow J$ [44,51]:

$$\begin{aligned} \frac{d\sigma}{d\Omega}^{J'\leftarrow J}(\hat{k}\hat{r}) &= \left(\frac{d\sigma}{d\Omega}^{J'\leftarrow J}\right)^{FBA} \\ &+ \sum_L \left[A_L^{J'\leftarrow J} - \left(A_L^{J'\leftarrow J}\right)^{FBA}\right] P_L(\cos\theta). \end{aligned} \tag{13}$$

The latter is a modified version of the series expansion (Eq. (12)) used for the DCS of non-polar systems and contains now three terms. The first one is the value of the DCS from the *rotating* dipole scatterer in the FBA, while the brackets contain the difference between the A_L coefficient constructed via the ab initio computed K-matrix as obtained from the propagation of the wavefunction in the coupled equation (10) for low partial waves plus the FBA $K_{\ell\ell'}$ elements for larger partial waves, and the A_L coefficients entirely provided by the FBA approximation for the fixed dipole scatterer [44,49,51].

It is important to remember that there is no one-to-one correspondence between L and ℓ, although we note that each A_L is a quadratic form of the *transition* matrix T, linked to the scattering S matrix and to the reactance K

Table 1. Computed rotational constants for phenyl (left column) and o-benzyne (right column). See text for further details.

	C_6H_5	C_6H_4
A	6.3875 GHz = 2.6417e-05 eV	7.2137 GHz = 2.9834e-05 eV
B	5.7178 GHz = 2.3647e-05 eV	5.8100 GHz = 2.4028e-05 eV
C	3.0171 GHz = 1.2477e-05 eV	3.2181 GHz = 1.3309e-05 eV

matrix as

$$T = S - 1 = \frac{1 + iK}{1 - iK} - 1 \tag{14}$$

so that, generally speaking, it is possible to write

$$A_L = T^T X_L T, \tag{15}$$

where X_L is a symmetric matrix containing coupling terms depending on the rotator symmetry that arise by angular momentum algebra [52]. Since each A_L has a clear interference contribution term involving $K_{\ell,\ell'}$ elements from the larger partial-waves (which for $\ell > \ell_B$ are susceptible to be replaced by the FBA $K_{\ell,\ell'}$ elements) and those corresponding to small partial waves (which for $\ell < \ell_B$ cannot be treated in the same way as the previous ones), in the closure formula of equation (13) particular attention should be paid to the convergence of both the label L and the value of ℓ_B, the latter being related to the number of partial waves mixed in by the incoming electron and not treated in the FBA approximation.

All the above considerations, as it will become evident below, are driven by the necessity of providing numerically reliable values of the ICS down to electron temperatures of a few Kelvin, as those encountered in the interstellar medium within the electron energy distribution functions that are expected to exist in those environments. This means that our aim of generating accurate attachment rates at those temperatures shall require on our part a very careful analysis of the DCS calculations which preceed that computational step.

4 Results and discussion

4.1 Numerical details

The molecular orbitals of the equilibrium structure of the target molecule were obtained at the ROHF (for the phenyl radical) and at the HF level (for the o-benzyne) by using the aug-cc-pVTZ basis set [53]. These ab initio calculations constitute the starting point of the SCE expansion, as briefly described in the previous section, and produce a total SCF energy of –230.129212 and 229.467987 hartrees for the neutral phenyl radical and for the neutral closed-shell orthobenzyne, respectively.

Using the above basis set, the computed neutral electronic molecular wavefunction yields a permanent dipole moment of 0.7348 $D = 0.290$ a.u. and a tensorial polarizability which components are 44.05, 82.02 and 77.68 Bohr^3 (xx, yy and zz, respectively) for the open-shell phenyl. On the other hand, for the permanent dipole moment as well as for the spherical polarizability of the orthobenzyne we use here the theoretical values that were calculated by us at the same basis set expansion level ($1.77D = 0.696$ a.u. and 67.64 a.u.^{3}, which is the spherical dipole polarizability) in previous work [31].

When considered in terms of rigid rotor classification, the two molecules belong to the C_{2v} symmetry group (the highest rotational symmetry axis is a binary one, placed in both cases along the molecular plane), so that in terms of rigid rotor classification, they are both asymmetric rotors. The associated rotational constants were computed by us by using the GAUSSIAN suite of ab initio quantum chemistry codes [53] at the same basis set expansion level as for the dipole and for the polarizability, as summarized in Table 1.

Following the conventional chain of inequalities $I_A \leq I_B \leq I_C$ of the three moments of inertia, we clearly see that in both molecules there is a marked difference between the first two rotational constants (A and B, corresponding to the smaller moments of inertia) and the third one, C. Accordingly, in order to simplify the calculation of the differential cross section for rotational excitation, we describe both the target systems as *oblate* symmetric rotors ($I_A = I_B \leq I_C$), hence using the average value of the larger constants (A, B), while keeping the smaller one unchanged. We have computed the DCS for the rotationally elastic and inelastic channels using the simpler basis set of symmetric rotational eigenfunctions [52]

$$\psi^{symm}(\alpha\,\beta\,\gamma) = \left(\frac{2J+1}{8\pi^2}\right)^{1/2} \mathcal{D}^{J*}_{M_J K_J}, \tag{16}$$

characterized by the three rotational quantum numbers J, K_J and M_J [54], $\mathcal{D}$ being the Wigner rotation matrix [54]. The above choice alters very little the final scattering quantities employed in the present discussion.

The final (converged) scattering parameters used throughout the present work can be summarized as follows:

(i) $\ell_{Max} = 50$ as the maximum angular value for the partial waves used in the scattering wavefunction expansion needed to solve the coupled equations (10);
(ii) $\ell_V = 100$ as the maximum angular value for the partial waves to expand the interaction potential V_{SMECP}, as described in the previous section;
(iii) $\ell_{FBA} = 34$ as the maximum angular value for the FBA corrected partial waves: it means that 1225 $K^{FBA}_{\ell,\ell'}$ elements are used in evaluating the A^{FBA}_L coefficients;
(iv) $\ell_{MaxK} = 17$ as the maximum ℓ value to represent the ab initio scattering K-matrix used in the closure formula (Eq. (13)): this number physically refers to the maximum angular value ℓ_B for the undeformed

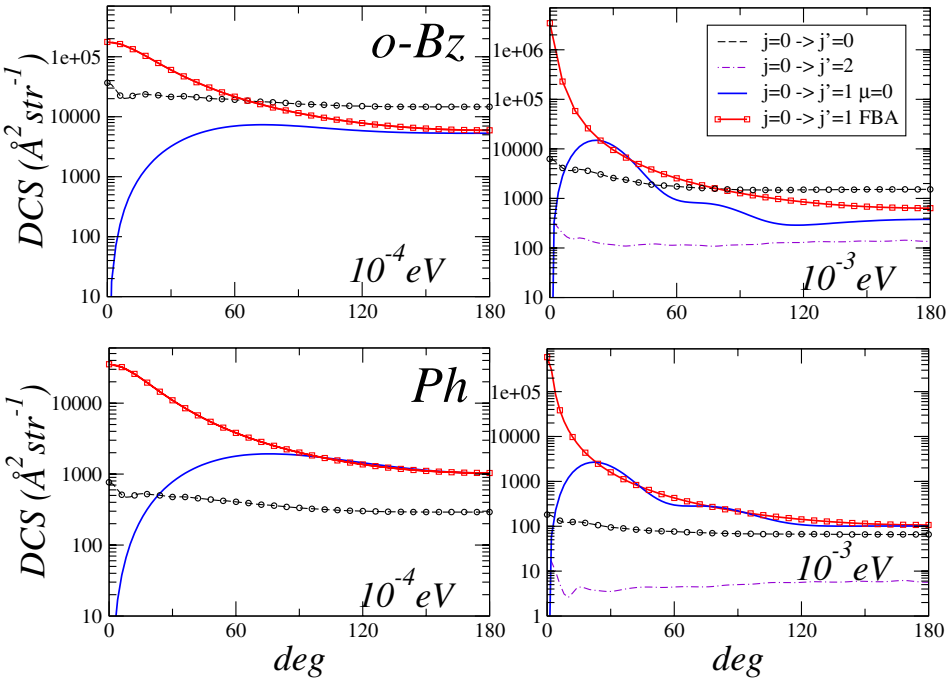

Fig. 1. Computed differential cross sections for the electron-benzyne collision (upper panels) and for the electron-phenyl collision (lower panels) at 10^{-4} eV and 10^{-3} eV, respectively. See main text for further details.

partial waves used in the calculation of the A_L coefficients in equation (13)

(v) $L = 68$, the maximum L in the series expansion (Eq. (13));

(vi) 500 Å, the size of the physical 'box' through which we propagate the scattering (unknown) radial wavefunction $f_{h\ell}^{p\mu}(r)$ to produce the relevant ab initio $K_{\ell,\ell'}$ elements.

4.2 Evaluating the electron's quantum deflection at low energies

In this section we present our findings on the efficiency of electron's deflection at low energies for both molecules in the gas-phase. We include the corrective terms which account for the long-range dipolar interaction as treated in the framework of the FBA approximation discussed before.

Figures 1–3 show our results for the computed state-to-state DCS of electron-phenyl (lower panels in each figure) and electron-orthobenzyne collisions (upper panels). In addition to the pure elastic collisions $|J' = 0\rangle \leftarrow |J = 0\rangle$, the first two rotational excitations starting from the rotational ground state $|J = 0\rangle$ are reported.

One should note that the energy window covers here the low-energy region and goes beyond it down to the ultra-low energies (10^{-3} and 10^{-4} eV): it is thus important to discuss the range of validity of the FBA. The early analysis by Takayanagi [55] found that, in the case of relatively small permanent dipole moments ($\mu \leq 1$ a.u. $= 2.54$ D) the partial waves describing the colliding electron are distorted so little that they can be efficiently treated in the perturbative Born theory. In fact, it can be shown that when the ratio between the colliding electron energy (in the meV range and below) and the energy transferred in the collision itself (via rotational excitations) is large, the contributions of higher partial waves continue to be present, so that the Born method gives reliable results for the DCS for such external contributions. For rotational transitions having the rotational ground state as the initial state, this is then expressed with the following formula [49,52]:

$$\left(\frac{d\sigma}{d\Omega}^{J'\leftarrow J}\right)^{FBA} = \frac{4}{3}\frac{k'}{k}\mu^2\frac{2J'+1}{k^2+k'^2-2kk'\cos\theta} \times \begin{pmatrix} J & J' & 1 \\ K_J & -K_J & 0 \end{pmatrix}^2, \quad (17)$$

which depends on the squared value of the permanent dipole (μ) but does not depend on the K-matrix since it is derived by using the point dipole model (k and k' being the electron linear momenum before and after the collision, while J/J' and K_J refer to the initial/final rotational quantum number and its projection on the main molecular symmetry axis, respectively). Furthermore, since the short range interactions between the incoming electron and the molecular target affect only the small ℓ partial waves, the previous conclusions also apply, so that the inaccuracy introduced by equation (17) to compute the DCS in the ultra-low energies regime (i.e. 10^{-4} and 10^{-3} eV; see the DCS for the $|J = 1\rangle \leftarrow |J = 0\rangle$ rotational transition reported by the red squares in Fig. 1) should not be unduly large.

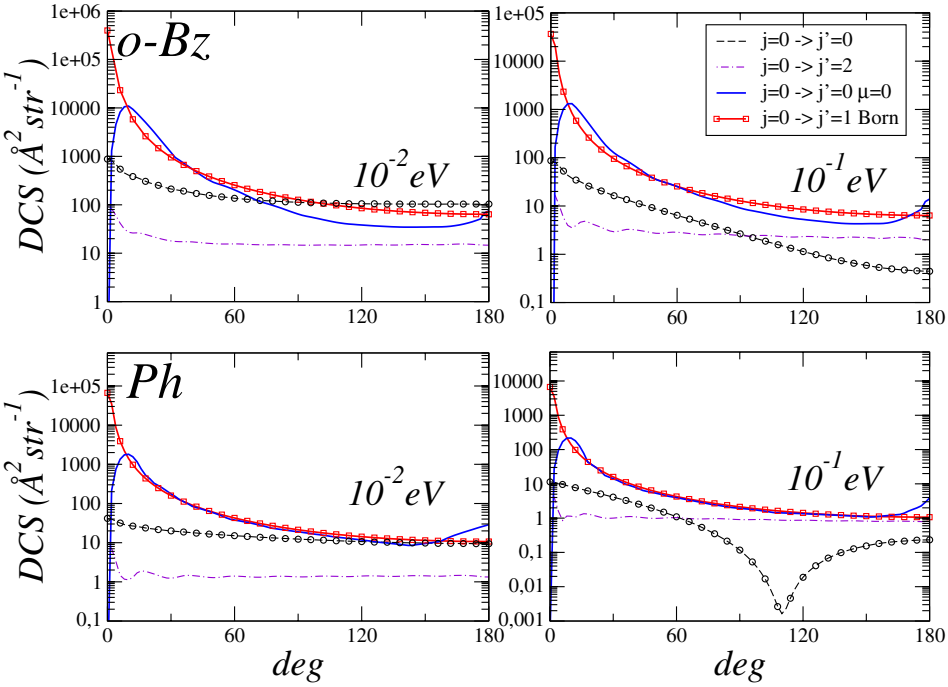

Fig. 2. Same as in Figure 1, but for 10^{-2} and 10^{-1} eV. See main text for further details.

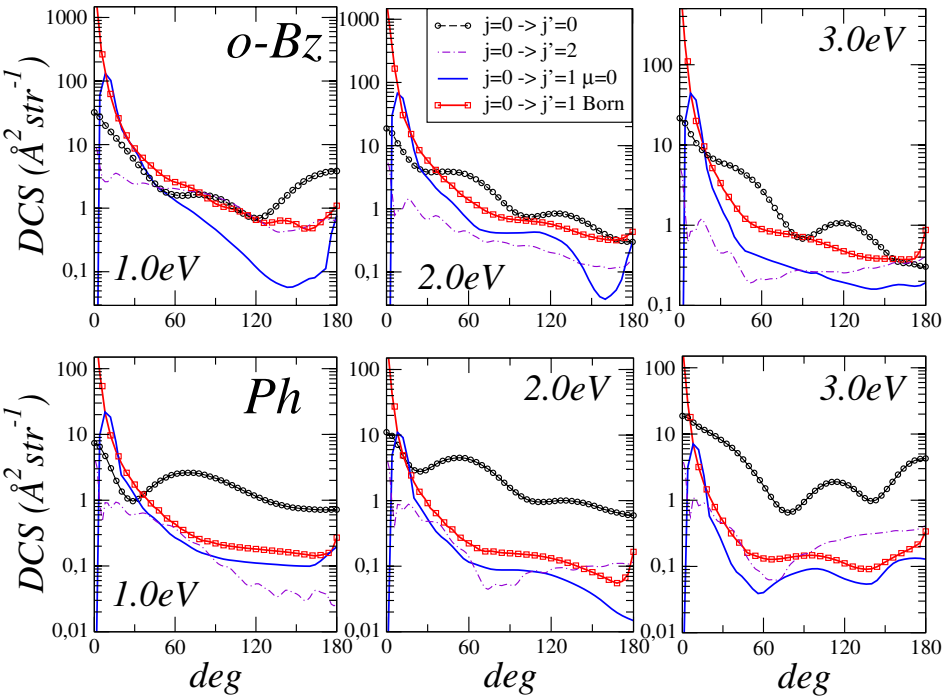

Fig. 3. Same as in Figure 1, but for 1, 2 and 3 eV. See main text for further details.

In this connection, it is possible to show that the DCS does not depend on the initial rotational state of the molecular target unless the scattering angle is very small [56]. Hence, when the collision energy decreases the 'critical' angle increases, so that the additional neglect of the molecular excitation temperature would become questionable. In the present case, due to the large moments of inertia for both molecular targets, the rotational excitation energy for the $|J' = 1\rangle \leftarrow |J = 0\rangle$ channel is so small that the critical angle remains small even at the collision energy of 10^{-4} eV, the smallest value computed here. At that ultra-low energy we have additionally extrapolated the DCS to angles below ∼4° by using an Akima-type spline fitting in order to better represent the marked peak in the forward direction shown by the DCS. One should mention that recent theoretical investigations [57]

on a different system showed that the ANR approximation is surprisingly effective even near threshold, hence at least qualitatively supporting the use of this approximation in the present work.

Generally speaking, it is well-known that when the collision energy moves down to vanishing values, the scattering is expected to be dominated by the $\ell = 0$ partial wave: accordingly, our results for both the title systems show a largely isotropic behavior (s-wave) of the $|J' = 0\rangle \leftarrow |J = 0\rangle$ differential cross section at 10^{-4} and 10^{-3} eV. This state-to-state DCS is evaluated according to equation (12) by using the ab initio computed K-matrix elements.

When the collision is treated in the FBA coupling scheme, the angular momentum ℓ of the incoming electron must change by ± 1 which therefore means that the main contribution to the scattering comes from the outgoing s-wave which is associated with the incoming p-wave, the latter being coupled by the dipole. Hence, when the collision energy is very small, it makes sense to assume that, even if the p-wave cannot penetrate the inner region, it still undergoes a small dephasing which arises from the long-range dipolar contribution and which, at least qualitatively, can justify the marked forward scattering at small angles for the $|J' = 1\rangle \leftarrow |J = 0\rangle$ rotational transition.

Similar considerations also hold when the incoming electron energy is increased to 10^{-2} and 10^{-1} eV: the panels in Figure 2 clearly show that the collisional event still continues to be dominated by the forward scattering for the rotational transition $|J' = 1\rangle \leftarrow |J = 0\rangle$ associated with the dipole. To produce the DCS for these energies we have now used the entire expression reported in equation (13). At the same time, we deem important to note that the largely isotropic behavior associated with the electron scattering in the $|J' = 0\rangle \leftarrow |J = 0\rangle$ rotational channel starts to breakdown when the energy is raised to 10^{-1} eV: at this energy value the short-range interactions couple in more partial waves which describe the incoming electron, so that the deflection of the latter is now given by superpositions of several partial waves and their interference leads to a deflection which is now angle-dependent.

When the collision energy is further increased to 1 eV and over, the interaction between the incoming electron and the targets is such that for both molecules new resonant features arise. We have already discussed elsewhere [31,41] the formation of transient anionic species, while our main interest here is instead on the angular redistributions of the scattered electrons as a function of the collision energy. Since we know that the elastic angular distributions can be used as a probe for the interaction potential, we see that both the C_6H_4 and the C_6H_5 are characterized by a marked forward scattering, thus the long-range dipolar interaction is still playing a dominant role. The two single-ring aromatic systems differ instead when the backward scattering behavior is analysed: it is indicative of an interaction mainly involving short-range potential terms, and accordingly it is associated with the resonant capture of the incident electron. For the orthobenzyne it arises at about 1 eV (for which we locate a σ^*-like b_2 resonance, see [31]) while for the phenyl we have shown [41] that at 3 eV such a behavior is chiefly linked to the π^*-like b_1 resonance found at 2.95 eV.

We have also computed the DCS (reported in Figs. 1−3 as blue solid lines) by neglecting the dipole moment correction: once the dipole interaction is taken out, the increasing behaviour at small angles is largely absent at very low energies while it produces a marked broad peak in the same angular region when the collision energy is increased from 10^{-3} eV to 3 eV. As will be discussed in more detail in the next section, the presence of a true dipole potential has strong effects on the associated ICS since larger ICS values will be obtained once the DCS with $\mu \neq 0$ are integrated all over the solid angle, thus greatly affecting the rate coefficients for low electron's temperatures.

4.3 The computed attachment rate coefficients

The elastic integral cross sections (ICS), as well as the momentum transfer cross sections (MTCS) have been computed from the state-to-state DCS discussed in the previous section via a trapezoidal integration and then by summing over the rotational transitions. They refer to the following scattering events

$$\begin{aligned} C_6H_5(X^2A_1) + e^- &\rightarrow \left(C_6H_5^-\right)^* \rightarrow C_6H_5^-/C_6H_5^* + e^- \\ C_6H_4(X^1A_1) + e^- &\rightarrow \left(C_6H_4^-\right)^* \rightarrow C_6H_4^-/C_6H_4^* + e^- \end{aligned} \quad (18)$$

and, in general terms, they describe two possible decay processes: once the metastable transient negative ion (TNI) is formed, in fact, it can either (i) decay into a bound anion or (ii) undergo autodetachment with concurrent excitation of molecular rotations. The resultant energy behaviour for both the ICS and the MTCS is shown as a function of the electron collision energy in Figure 4 (where the solid lines refer to the ICS for the two molecular systems and the dashed lines are for the MTCS): the rapidly increasing values of the ICS at low, and expecially at ultra-low energies, clearly indicate that the slowest component of the impinging electrons strongly interact with both gaseous molecular targets, a distinctive feature which was already visible by analyzing and discussing the DCS behavior in the same energy region.

Our estimates for the anion formation rate coefficients as a function of the kinetic electronic temperature T_e, are obtained by integrating the computed ICS over the energy distribution of the scattered electron. The latter is assumed to be thermalized and then expressed as a Boltzmann exponential

$$k_{EA}(T_e) \sim k_{TNI}(T_e) = \sqrt{\frac{8K_BT_e}{\pi\mu}} \frac{1}{(K_BT_e)^2} \times \int_0^\infty \sigma(E) E e^{-\frac{E}{K_BT_e}} dE. \quad (19)$$

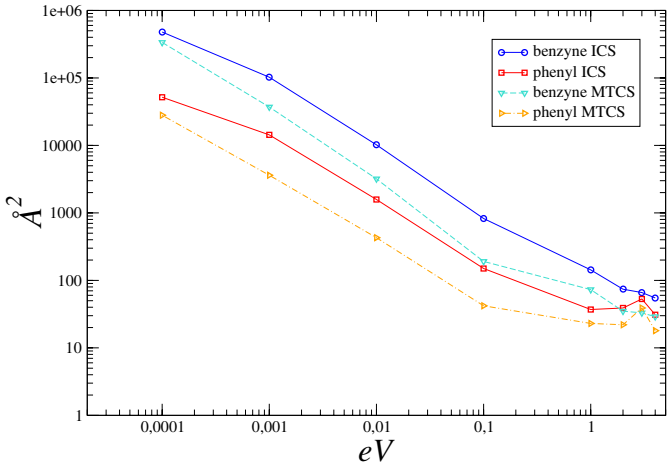

Fig. 4. Computed integral cross sections (soldi lines) and momentum transfer cross sections for the orthobenzyne (blue circles and light blue down triangles, respectively) and for the phenyl radical (red squares and orange right triangles, respectively). See main text for further details.

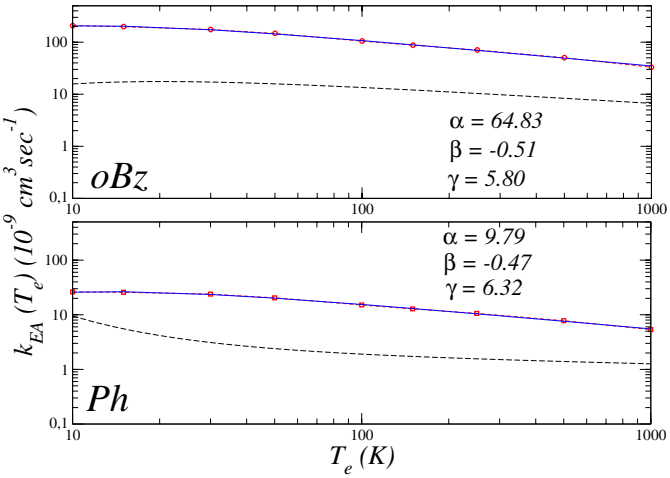

Fig. 5. Computed electron attachment rates for orthobenzyne and phenyl polar aromatic molecules. The corresponding fitting parameters for the Kooij-Arrhenius formula are also given in the figure. Here, α is in units of 10^9 $\mathrm{cm}^3\,\mathrm{sec}^{-1}$ and γ is expressed in temperature units, K. The dashed curves are the earlier calculations from [58].

As already explained in [58], the above equation refers to a general definition of the attachment rates and requires the further analysis and definition of the corresponding attachment cross sections on the r.h.s. of the equation itself. We remind the readers, already at this initial stage, that the present attachment rates shall be directly linked to our computed rates of formation of the TNI complex, as further discussed below. In the present analysis, in fact, our computed total cross section is made up of different processes that take place via binary collisions and which can lead to the formation of anionic metastable species (TNIs), the latter being therefore the cornerstone species that, from a kinetics point of view, leads in turn to the stable, bound negative ions. They will be discussed in greater detail in the following part of the present subsection.

The present rate coefficients k_{EA} describing the efficiency of electron attachments to form $(C_6H_5^-)^*$ and $(C_6H_4^-)^*$ are reported in Figure 5 as a function of T_e: the upper panel of that figure (red diamonds) refers to the k_{EA} values computed for the orthobenzyne system, while the lower one contains our k_{EA} for the phenyl radical (red squares). The blue line in each panel within the same figure shows the non-linear fitting of our computed rate coefficients according to the well-known Kooij-Arrhenius formula

$$k(T) = \alpha\,(T/300)^{\beta}\exp\left(-\gamma/T\right) \qquad (20)$$

which enabled us to produce the parameters $\alpha\,(\mathrm{cm}^3\,\mathrm{sec}^{-1})$, $\beta\,(\text{pure number})$ and $\gamma\,(\mathrm{K})$, also reported in the same Figure 5.

The dashed curves in both panels refer to the earlier calculations for the same quantities reported in [58].

The convolution of equation (19) over the electronic temperature T_e of the integral, total cross sections $\sigma(E)$ takes into account all metastable attachment processes over the relevant energy range, further including the sum over rotational excitation processes occurring from the rotational ground state, $|J = 0\rangle$; however, they do not include the channels involving either electronic or vibrational excitations. We know from previous analysis of polyatomic targets that the vibrational inelastic cross sections at the relevant energies account for approximately 10% of the integral cross sections so that they would not dramatically affect the values of $\sigma(E)$ in equation (19) [59]. One should additionally note that when the ultra-low energies are considered, as we also do in the present case for T_e below 50 K, the numerical convolution of equation (19) covers a very small energy field where the numerical value of the Boltzmann exponential function is still different from zero and where both the vibrational and the electronic excitation channels are clearly closed during the collisions.

In this framework, it is useful to look at the electron-attachment process

$$M(R_i) + e^- \xrightarrow{k_{EA}} M(R_f)^- \qquad (21)$$

more in detail, so that it can be divided into a first attachment stage (the TNI formation) and a subsequent one that, via multidimensional IVR, will produce a stable anion; thus, the overall process could be described by the following prototypical steps

$$M(R_i) + e^- \xrightarrow{k_{TNI}} \left[M^-\right]^* \xrightarrow{k_\alpha} M(R_f)^-, \qquad (22)$$

where M stands for the undissociated neutral molecular target, R_i (R_f) indicate the initial (the final) molecular geometry and k_α describes different stabilization paths, one of which is indeed the radiative stabilization channel

$$\left[M^-\right]^* \xrightarrow{k_{rs}} M(R_{rs})^- + h\nu \qquad (23)$$

while another is the dissociative attachment channel in which the dehydrogenation process leading $C_6H_5^-$ could have happened from benzene + e^-. Note that both are in

competition with the autodetachment process, namely

$$\left[M^-\right]^* \xrightarrow{k_{ad}} M(R_{ad}) + e^-. \tag{24}$$

In the above equations, we have indicated the deformations in the molecular structure as R_{rs}, R_{ad} and more in general as R_f depending on their occurrence via radiative stabilization (RS), via autodetachment (AD) or via stabilization by internal excitations. The latter path includes both dissociative attachment, DEA, and dipole bound state formation via low-energy dipole scattering states, DSS, as discussed in [41,60]. Since all the present calculations where performed at the equilibrium geometry, it therefore follows that R_i is at the minimum nuclear energy for each of the neutral polar aromatic molecules. On the basis of the above considerations, the calculations presented in this work generate from first principles all the states which are then expected to take part into the anion formation rate, k_{EA}, by including all the threshold resonances and virtual states that may occur when the collision energy gets close to threshold.

The final rate of electron attachment k_{EA} is associated with the rate coefficients for the TNI formation (k_{TNI}), as well as with both the k_{rs} and k_{ad} coefficients

$$k_{EA} = \left(\frac{k_{rs}}{k_{ad} + k_{rs}}\right) k_{TNI}, \tag{25}$$

when a steady state is assumed for the anionic formation [61]. The above relation is obviously valid within the largely collisionless environments of the ISM which we intend to consider in the present work. Furthermore, due to the fact that both k_{ad} and k_{rs} are positive quantities, one can further write

$$k_{EA} < k_{TNI}, \tag{26}$$

so that the kinetic parameter we try to evaluate, k_{EA}, has an upper bound in the rate constants that we calculate by including all resonant and dipolar processes within the relevant ICS, i.e. the k_{TNI}. It would be obviously useful to be able to estimate more accurately the relative sizes of the quantities of equation (26). However, their actual computations from quantum methods are currently out of reach for polyatomic molecules like those discussed in the present work. Additionally, and as mentioned earlier, since the vibrational relaxation channels are not included, we are somewhat limiting the available phasespace for the RS processes contributing to the k_{rs} coefficient, thereby reducing the value of the true k_{EA}, a situation which may help to partly offset the differences present between the terms of equation (26). Hence the present calculations, besides suggesting the mechanisms which are likely to play a role in the formation of the stable anions, are so far the only calculations which may be able to provide realistic cross sections which in turn enable us to yield practical values for the electron attachment rates, k_{EA}.

By looking at Figure 5 one immediately realizes that, moving from 1000 K down to 10 K, the rate constants for each of the two species increase by an order of magnitude. Such a behaviour is a consequence of the presence of the permanent dipoles which cause the integral cross section close to zero to be markedly larger. As the same figure also clearly shows, our computed rate coefficients, $k_{EA}^{C_6H_4}(T_e)$ and $k_{EA}^{C_6H_5}(T_e)$, follow a similar trend for the whole temperature window, since they both increase as the kinetic electronic temperature decreases from 1000 K to the value of 10 K, the latter being important in connection with special astrophysical environments as cold and dark molecular clouds.

In relation to our earlier, more approximate estimates of k_{EA} values [58] (reported in Fig. 5 as dashed lines), we see that the present calculations produce attachment rates which are larger by almost an order of magnitude over the whole temperature region (10 K $< T_e <$ 1000 K).

The differences between the present k_{EA} values and those of references [31,58] are due to the improvements in the present study via a more numerically extensive inclusion of the dipole effects. As discussed earlier, in fact, in order to treat the dipole interaction correctly, we had to markedly increase the size of the physical region where the interaction potential is evaluated, which implies to consider a larger number of partial waves. The key to understand the differences between the present rates and those reported in [58] can be found in the fact that by using the FBA approach we are no more required to use a large set of partial waves to compute the K-matrix, while the spatial region where the smaller set of $K_{\ell\ell'}$ elements are numerically computed must be extended so that the dipole effects are fully included in the ab initio K-matrix which represents the starting point for the FBA approach.

It is also interesting to note that the results of the present study are in keeping with what we have found with a similar set of calculations involving polar polyynes, C-rich chains [60], where rates of the same order of magnitudes were indeed found.

5 Present conclusions

In this work we have analyzed in great detail the effects and consequences of the permanent dipole moments on the interaction between ambient free electrons and gas-phase phenyl and benzyne molecules, taken to represent two prototypical, single ring, aromatic PAHs. The object of this theoretical and computational study was to understand the behavior of electron deflection functions (in quantum terms, their angular distributions after scattering off the target molecules) over a broad range of possible energies within those expected to play a role in protoplanetary atmospheres and in early star formation processes, as discussed in the introduction to this paper.

We were also interested in analyzing more in detail the effects of the permanent dipole-charge potential terms on the final electron attachment rates which could be obtained from our calculated integral, elastic and rotationally inelastic, cross sections for both systems and to produce a realistic analytic representation of such rates over a broad range of temperature as requested from their possible use within evolutionary modelings of the specific

ISM regions where such processes would be relevant (e.g. see [58]).

The new calculations on the angular distributions reveal the crucial importance of dipole-charge interactions in the forward direction and especially at the very-low electron energies necessary to reach the low temperature ranges (below 100 K) needed to model the corresponding attachment rates of this study. They further show that, using a carefully selected range of angles, allows one to safely employ the FBA scheme to generate the forward scattering cross sections even at the lowest scattering energies reached in this study. The angular distributions also show clearly that both low energy electrons, and more energetic free electrons which may be present in the ISM environment, will be mostly scattered in the forward direction, thus showing very little distortion of the free electrons' distribution, and therefore of its effects on the magnetic environments, where these polar molecules would be present. The only presence of marked, but not dominant, backward scattering was found by our calculations within the energy regions close to the resonant attachment processes which exist in both molecules at the higher energies of the incoming electrons.

Another significant result of the present calculations deals with the generation of electron attachment rate values, k_{EA}, from a convolution over the examined range of collision energies of the integrated angular distributions. The final cross sections include the elastic, resonant components and the rotationally inelastic components since nothing is known about the vibrational distributions in the molecular targets nor on their electronic state composition. It is, however, reasonable to assume that at the temperatures of interest both species would be in their ground electronic and vibrational states, hence our present choice of scattering channels contributions.

The newly calculated attachment rates turn out to be larger over the whole range of temperatures, in comparison with our previous calculations of the same quantities [58] where, however, the long-range effects of the dipolar interactions on the K-matrix calculations had only been included in a limited form and the detailed analysis of the consequences of permanent dipoles on scattering observables carried out in the present work had not yet been done.

It is interesting to note that the present attachment rates are, however, in close agreement with similar rates obtained recently for linear, C-rich molecules [60] and essentially scale with the size of the dipole moments of the target molecules, especially in the very-low temperature range.

The present work therefore shows that, because of their polar nature, both molecules analysed here constitute very good candidates for the production of stable anions in the chemistry of early star formations and in protoplanetary atmospheres. The latter charged species could in turn, as discussed earlier, take part in the efficient chemistry of condensation reactions between anionic and cationic species that can in turn drive the growth of larger PAHs in the ISM environment.

The financial support from the University of Rome Research Committe and the computational facilities of the CINECA Consortium are gratefully acknowledged.

References

1. A.G.G.M. Tielens, *The Physics and Chemistry of the Interstellar Medium* (Cambridge University Press, 2005)
2. A.G.G.M. Tielens, EAS Pub. Ser. **46**, 3 (2011)
3. F. Salama et al., ApJ **728**, 154 (2011)
4. C.W. Bauschlicher et al., ApJS **189**, 341 (2010)
5. T.P. Snow, V.M. Bierbaum, Annu. Rev. Anal. Chem. **1**, 229 (2008)
6. J.P. Maier et al., ApJ **726**, 41 (2011)
7. T. Oka, B.J. McCall, Science **331**, 293 (2011)
8. J. Cernicharo et al., ApJ **546**, L123 (2001)
9. P. Ehrenfreund, A.M. Sephton, Faraday Discuss. **133**, 277 (2006)
10. A.G.G.M. Tielens, in *Proc. of the IAU Symposium*, edited by J. Cernicharo, R. Bachiller (Cambridge University Press, 2011), Vol. 280
11. S. Kwok, *The origin and evolution of planetary nebulae*, in Cambridge Astrophysics Series (Cambridge University Press, 2000)
12. S. Kwok, ApJ **198**, 583 (1975)
13. K. Volk, G.Z. Xiong, S. Kwok, ApJ **530**, 408 (2000)
14. L. Ziurys, Proc. Natl. Acad. Sci. **106**, 12274 (2006)
15. E. Josselin, R. Bachiller, A&A **397**, 659 (2003)
16. S. Kwok, *Organic matter in the Universe* (Wiley-VCH, 2012)
17. J.H. Black, in *Proc. of the IAU Symposium*, edited by J. Cernicharo, R. Bachiller (Cambridge University Press, 2011), Vol. 280
18. D.M. Hudgins, L.J. Allamandola, A&A **516**, L41 (1999)
19. S. Kwok, K. Volk, P. Bernath, ApJ **554**, L87 (2001)
20. M. Frenklach, E.D. Feigelson, ApJ **341**, 372 (1989)
21. H. Wang, M. Frenklach, J. Phys. Chem. **98**, 11465 (1994)
22. I. Chechneff, J.R. Barker, A.G.G.M. Tielens, ApJ **401**, 269 (1992)
23. H. Wang, M. Frenklach, Combust. Flame **110**, 173 (1997)
24. N.W. Moriarty, M. Frenklach, Proc. Combust. Inst. **28**, 2563 (2000)
25. A. Comandini, K. Brezinsky, J. Phys. Chem. A **115**, 5547 (2011)
26. E.R. Micelotta, A.P. Jones, A.G.G.M. Tielens, A&A **510**, A36 (2010)
27. D.S.N. Parker, F. Zhang, Y.S. Kim, R.I. Kaiser, A. Landera, V.V. Kislov, A.M. Mebel, A.G.G.M. Tielens, Proc. Natl. Acad. Sci. **109**, 53 (2012)
28. E.R. Micelotta, A.P. Jones, A.G.G.M. Tielens, A&A **510**, A37 (2010)
29. E.R. Micelotta, A.P. Jones, A.G.G.M. Tielens, A&A **526**, A52 (2011)
30. I. Cherchneff, EAS Pub. Ser. **46**, 177 (2011)
31. F. Carelli, F. Sebastianelli, I. Baccarelli, F.A. Gianturco, ApJ **712**, 445 (2010)
32. F. Carelli, F. Sebastianelli, M. Satta, F.A. Gianturco, Mon. Not. Roy. Astron. Soc. **415**, 425 (2011)
33. R.F. Gunion, M.K. Gilles, M.L. Polak, W.C. Lineberger, Int. J. Mass Spectrom. Ion Proc. **117**, 601 (1992)
34. P.G. Wenthold, R.R. Squires, W.C. Lineberger, J. Am. Chem. Soc. **120**, 5279 (1998)
35. R.J. McMahon et al., ApJ **590**, L61 (2003)
36. E. Kraka, D. Cremer, Chem. Phys. Lett. **216**, 333 (1993)

37. S. Lepp, A. Dalgarno, ApJ **324**, 553 (1988)
38. V. Wakelam, E. Herbst, ApJ **680**, 371 (2008)
39. E.L.O. Bakes, A.G.G.M. Tielens, ApJ **499**, 258 (1998)
40. M. Hammond, A. Pathak, A. Candian, P.J. Sarre, EAS Pub. Ser. **46**, 373 (2011)
41. F. Carelli, M. Satta, F.A. Gianturco, Eur. Phys. J. D **67**, 230 (2013)
42. N.J. Demarais, Z. Yang, O. Martinez Jr., N. Wehres, T.P. Snow, V.M. Bierbaum, ApJ **746**, 32 (2012)
43. R.R. Lucchese, F.A. Gianturco, Int. Rev. Phys. Chem. **15**, 429 (1996)
44. F.A. Gianturco, P. Paioletti, in *Novel aspect of electron-molecule collisions*, edited by K.H. Becker (World Scientific, 1998)
45. N. Sanna, F.A. Gianturco, in *Photon and Electron Collisions with Atoms and Molecules*, edited by P.G. Burke, C.J. Joachain (Plenum, New York, 1997)
46. S.L. Altman, A.P. Cracknell, Rev. Mod. Phys. **37**, 19 (1965)
47. R.R. Lucchese et al., 'ePolyScat' program, version E2 (1993)
48. S. Hara, J. Phys. Soc. Jpn **22**, 710 (1967)
49. N. Sanna, F.A. Gianturco, Comput. Phys. Commun. **114**, 142 (1998)
50. S. Altshuler, Phys. Rev. **107**, 114 (1957)
51. D.W. Norcross, N.T. Padial, Phys. Rev. A **25**, 226 (1982)
52. F.A. Gianturco, A. Jain, Phys. Rep. **143**, 348 (1986)
53. M.J. Frisch et al., *Gaussian 03* (Gaussian Inc., Wallingford, CT, 2004)
54. R.N. Zare, *Angular Momentum: Understanding Spatial Aspects in Chemistry and Physics* (Wiley, 1986)
55. K. Takayanagi, J. Phys. Jpn **21**, 507 (1966)
56. Y. Okamoto, K. Onda, Y. Itikawa, J. Phys. B **26**, 745 (1993)
57. A. Faure, V. Kokoouline, C.H. Greene, J. Tennyson, J. Phys. B **39**, 4261 (2006)
58. F. Carelli, T. Grassi, F.A. Gianturco, A&A **549**, A103 (2013)
59. S. Irrera, F.A. Gianturco, New J. Phys. **7**, 1 (2005)
60. F. Carelli, T. Grassi, M. Satta, F.A. Gianturco, ApJ **774**, 97 (2013)
61. E. Herbst, Nature **289**, 656 (1981)